

Scalable Drift Monitoring in Medical Imaging AI

Jameson Merkow^{1,*†}, Felix J. Dorfner^{2,3,†}, Xiyu Yang^{2,3}, Alexander Ersoy¹, Giridhar Dasegowda^{2,3}, Mannudeep Kalra^{2,3}, Matthew P. Lungren¹, Christopher P. Bridge^{2,3,‡,+}, and Ivan Tarapov^{1,‡}

¹Microsoft Health and Life Sciences (HLS), Redmond, WA

²Department of Radiology, Massachusetts General Hospital, Boston, MA

³Harvard Medical School, Boston, MA

*jameson.merkow@microsoft.com

†cbridge@mgh.harvard.edu

‡these authors contributed equally to this work

‡Co senior authors

ABSTRACT

The integration of artificial intelligence (AI) into medical imaging has advanced clinical diagnostics but poses challenges in managing model drift and ensuring long-term reliability. To address these challenges, we develop MMC+, an enhanced framework for scalable drift monitoring, building upon the CheXstray framework that introduced real-time drift detection for medical imaging AI models using multi-modal data concordance¹. This work extends the original framework's methodologies, providing a more scalable and adaptable solution for real-world healthcare settings and offers a reliable and cost-effective alternative to continuous performance monitoring addressing limitations of both continuous and periodic monitoring methods. MMC+ introduces critical improvements to the original framework, including more robust handling of diverse data streams, improved scalability with the integration of foundation models like MedImageInsight for high-dimensional image embeddings without site-specific training, and the introduction of uncertainty bounds to better capture drift in dynamic clinical environments. Validated with real-world data from Massachusetts General Hospital during the COVID-19 pandemic, MMC+ effectively detects significant data shifts and correlates them with model performance changes. While not directly predicting performance degradation, MMC+ serves as an early warning system, indicating when AI systems may deviate from acceptable performance bounds and enabling timely interventions. By emphasizing the importance of monitoring diverse data streams and evaluating data shifts alongside model performance, this work contributes to the broader adoption and integration of AI solutions in clinical settings.

1 Introduction

The role of artificial intelligence (AI) in medical imaging has expanded significantly in recent years as evidenced by the increasing number of academic publications and the rising adoption of AI applications in clinical settings^{2–6}. To ensure the safe and effective use of these AI algorithms, researchers and clinicians are developing a broad set of evaluative and deployment best practices. These practices include “day 0” validation, which typically involves clinical evaluation against a reference set to assess AI model performance^{7,8}. As the field matures and clinical AI governance practices are being developed, there is growing recognition of the need for continuous, explainable monitoring tools that promptly address the risks of prediction drift, feature drift, and input data shifts^{9–11}. In particular, recent cases studies have highlighted the risk that such drift can lead to significant degradation of model accuracy following deployment^{12–14}.

Despite the recognized importance of continuous and explainable monitoring, many organizations rely on direct user reporting of model performance^{15,16}. While this offers an effective means aims to assess whether the model’s predictions remain accurate, it frequently fails to identify the root cause of performance changes such as changes in the input data. Moreover, direct performance monitoring requires timely access to ground truth labels, which are often provided manually, and as such monitoring continuously in this manner remains cost-prohibitive and may diminish the efficiency benefits of AI. If instead checks are performed periodically, the result may be delayed detection and response to issues.

A promising approach to overcoming the costs associated with direct performance monitoring involves monitoring for the changes in input data streams using fully automated methods. Previous studies and methodologies have made significant strides in the monitoring of machine learning models, however these primarily focus on other domains, for example the monitoring of Electronic Health Records (EHR) data^{17,18} and lack support for imaging data. Supporting imaging data often requires generating image embeddings to create low-dimensional summaries of images for the purpose of drift detection, with traditional approaches like Variational Autoencoders (VAEs)¹⁹ posing several challenges. VAEs require extensive site-specific

training, lack the expressiveness to capture the complexity of medical images, and may necessitate separate models for different modalities or locations. This increases operational complexity and computational burden, limiting scalability and adaptability across institutions with diverse imaging protocols.

The need for adaptive monitoring was particularly evident during the COVID-19 pandemic, which brought rapid changes to healthcare workflows and emphasized the necessity of robust monitoring systems. As clinical protocols evolved and healthcare staff faced increased workloads, automated monitoring became crucial in identifying subtle shifts and ensuring the continued effectiveness of medical imaging AI. However, beyond COVID-19, serial chest radiographs are common in hospitalized patients, and often have vast variations in acquisition techniques (projection - posterior-anterior versus anterior-posterior; portable versus non-portable acquisition devices and positions) and patient condition and abnormalities (variations in lung volumes, upright versus supine, rotation, support devices and catheters, and extent and type of abnormalities). These variations do make interpretation of radiographs subjective and error-prone for radiologists as well as challenge any AI tools. By providing real-time insights and easing the burden on medical professionals, these systems will play a vital role in navigating workload challenges while maintaining quality care.

Our prior work with CheXtray¹ addresses this gap by developing a framework to support the automated monitoring of medical imaging AI models designed to include comprehensive image data analysis. CheXtray introduced a novel metric called multi-modal concordance (MMC), which aggregates metrics from various sources to assess overall data drift, and crucially does not assume access to the ground truth labels needed to monitor model performance. In an experimental setting, MMC+ demonstrated a strong correlation with model performance when artificial drift was induced within a datastream. However, recent research has shown that real-world data is more complex, and relying solely on surrogate metrics like MMC for performance monitoring can be ineffective²⁰.

Building on our previous conference paper¹, this work presents several key contributions to the field of AI model monitoring for medical imaging, with a strong focus on real-world applications and advancements. In our previous work, we introduced the multi-modal concordance (MMC) metric; in this work, we present an updated version we refer to as MMC+ to differentiate between the original metric and the enhancements made here. Our research expands upon the initial CheXtray framework by (1) implementing improvements to existing methods, thereby enhancing overall system performance; (2) integrating a foundation model to generate powerful, pre-trained image embeddings, which addresses the limitations of traditional approaches like VAEs and significantly improves scalability and expressiveness across diverse imaging modalities; (3) conducting a comprehensive real-world test of the system during COVID-19, demonstrating its practical utility and effectiveness in clinical settings; (4) performing an in-depth analysis of MMC+ versus model performance, which provides valuable insights into their relationship; and (5) discovering that maintaining MMC+ within an optimal range is associated with stable and consistent AI model performance, reducing the need for direct performance monitoring. When MMC significantly deviates from this range, there is increased performance variability, signaling the necessity for a performance audit. These insights offer critical guidance for monitoring medical imaging AI models, helping to ensure reliable and accurate outputs in dynamic healthcare environments.

The implications of these findings are significant for the field of medical imaging AI, where data shifts can occur due to a variety of factors, such as changes in patient demographics, disease prevalence, and imaging protocols. By leveraging data drift monitoring, we can gain insight into different factors that drive change in model performance, helping us identify root causes, addressing gaps in many current monitoring solutions. This approach aligns with the need for a systematic, real-time performance monitoring framework that can adapt to the unique challenges posed by medical imaging data, ultimately supporting the broader adoption and integration of AI solutions in healthcare settings.

2 Materials and Methods

2.1 Metric Development and Calculation

In our previous work, we introduced the CheXtray framework, which laid the foundation for generating the multi-modal concordance (MMC) metric. In outline, MMC is an aggregate of distance measurements across multiple data elements including image metadata, image appearance, and model predictions, providing a single value representing the overall dissimilarity between two sets of medical exams. For each component data element, a unimodal distance metric is calculated using appropriate statistical methods. These distance metrics are then combined through a process of normalization, weighting, and aggregation to produce a unified MMC score.

In this work, we extend the CheXtray framework by developing MMC+, an enhanced version of the original metric. MMC+ introduces uncertainty bounds to the metric calculation, providing a more robust measure of drift that reflects uncertainty introduced by fluctuations in the number of samples over time and decoupling the measurement of distance from the estimation of its uncertainty. Additionally, we refine the framework by employing alternative methods for sampling, distance metrics, and weighting. We also replace the VAE used for image embeddings with a powerful foundation model, which generates highly expressive embeddings without the need for site-specific training. This shift improves the robustness and generalizability of the system across diverse medical imaging modalities. However, we maintain the same aggregation and normalization methods

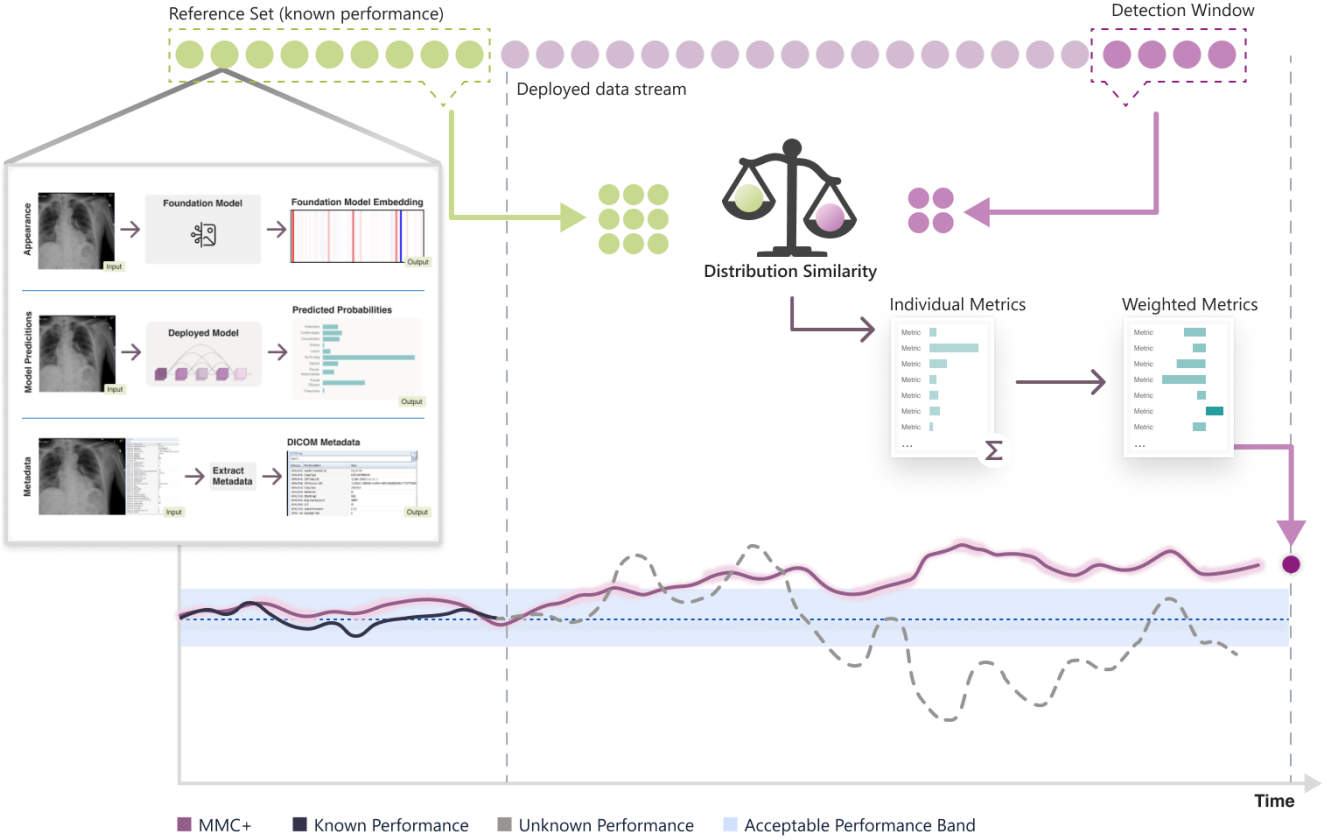


Figure 1. Illustration of the CheXStray framework for calculating the MMC+ metric. MMC+ is calculated by comparing a reference set with a detection window from ongoing data streams to assess distribution similarity. High MMC+ values indicate potential deviations from normal performance thresholds. The upper panel shows the steps for calculating MMC+ using components in three high-level categories: Appearance, Model Predictions, and Metadata. Each individual component's distribution is evaluated against the reference set to calculate a similarity metric. These metrics are then normalized and weighted to be aggregated into the MMC+ metric. The lower panel presents an example of MMC+ over time, displaying its relationship to known performance values and acceptable performance bands.

from the original framework, ensuring consistency while allowing for a more flexible and comprehensive evaluation of model drift. In the following sections, we highlight the details of these changes and remind the reader of relevant aspects of the CheXstray framework to provide a comprehensive understanding of the enhancements introduced in MMC+.

2.1.1 Drift Detection Window

The multi-modal concordance (MMC+) metric quantifies the degree of drift or change between a *reference window*, R , representing a dataset with well-characterized model performance, and a *detection window*, denoted by W , with unknown model behavior. The reference window is typically collected shortly before a model is deployed, using data with known ground truth to assess model performance. The detection window, on the other hand, consists of the set of samples within a sliding temporal window of fixed duration used to assess drift over time. If the MMC+ indicates a high level of dissimilarity between the detection window and the reference window, it suggests that the model is currently operating on data upon which its performance is not well characterized.

The detection window is defined by two key temporal parameters: duration and stride. The duration, τ , specifies the total length of time that each window covers, while the stride, δ , determines the time interval between the start of one window and the start of the next. As such, if a data stream consists of items x_i (each representing both an image and its associated metadata) arriving at time t_i , the detection window is constructed according to:

$$W_k = \{x_i \mid t_k - \tau < t_i \leq t_k\} \quad (1)$$

$$t_{k+1} = t_k + \delta$$

Each detection window W_k serves as the basis for which the MMC+ metric is computed. As the detection window slides

over time, new windows are generated at each step, enabling continuous monitoring of model performance. The MMC+ metric quantifies the drift between these detection windows and the reference window, providing a robust measure of how well the model is performing on current data relative to the established baseline. By systematically calculating MMC+ to each detection window, we can assess and track the stability of the data stream over time. For clarity, we drop the notation indicating the time at which the window was taken, as the metric calculation is generic with respect to time and does not depend on when the window was collected.

2.1.2 Distance Metrics

Distance metrics are the core component for quantifying the difference between the reference and detection windows. The original MMC metric relied on two univariate statistical tests for this purpose: the χ^2 (chi-squared) test for categorical (discrete) variables and the Kolmogorov-Smirnov (KS) test for continuous variables. However, further experimentation revealed several limitations in these choices, prompting us to explore alternatives for the improved MMC+ metric.

For discrete variables, the χ^2 test poses several challenges. It has no defined value if a particular categorical/discrete value is present in the detection window but absent from the reference set, or vice versa, unless special heuristic corrections are applied. This issue is common in real-world scenarios, such as when new models of scanners or point-of-care devices are introduced in a hospital setting, and thus any effective distance metric must address this in a principled way. Additionally, the χ^2 test is sensitive to sample sizes, often leading to inflated test statistics and distorted comparisons, especially when expected frequencies are high. Moreover, the test statistic itself is not designed to measure similarity between distributions, limiting its ability to quantify differences effectively. Finally, using statistical tests in general conflates the measurement of distance with the uncertainty around that measurement, which can blur the interpretation of results especially when sample sizes can vary considerably over time. These shortcomings make the χ^2 test a less suitable choice for distance or similarity measurement in our context.

The KS test, used for continuous variables, has further limitations. It is defined only for distributions over one-dimensional variables, which led MMC to measure distance independently along each dimension of any multi-dimensional real valued data. This approach overlooks potential shifts in the joint distribution of variables, which can be crucial in detecting changes in real-world applications where variables are interdependent and may disproportionately weight changes detected in individual variables. Additionally, the KS test measures the “vertical shifts” between probability distributions (i.e., the change in probability for a given value of the variable) without accounting for “horizontal shifts” (the shift in the variable’s value itself) and thus insignificant shifts in a continuous value can give rise to large measurements of distance if they are consistent across samples.

With MMC+, we tackle these limitations by using the Hellinger distance for univariate discrete variables and the Wasserstein distance for both uni- and multivariate continuous variables. These choices effectively resolve the issues posed by the χ^2 and KS tests. Both Hellinger and Wasserstein are robust statistical distance metrics, designed to quantify the dissimilarity between two distributions. Unlike the χ^2 test, the Hellinger distance handles small sample sizes and missing categories gracefully, providing a more reliable measure of similarity between distributions, even when certain values are absent in one set. Similarly, the Wasserstein distance overcomes the KS test’s limitations by capturing differences in both the “vertical” and “horizontal” dimensions, and is sensitive to shifts in the joint distribution of multivariate data.

In addition, both metrics are non-parametric, meaning they do not rely on assumptions about the underlying distribution’s form. This makes them suitable for a wide range of real-world data and allows us to calculate more consistent and interpretable results in complex healthcare environments.

More formally, for discrete variables (such as scanner model name or photometric interpretation) with K discrete values, we calculate distances between two generic sets of data points, $P = \{p_i\}_{i=1}^N$ and $Q = \{q_i\}_{i=1}^M$ where $p_i, q_i \in \{1, 2, \dots, K\}$, using the Hellinger distance²¹, which is defined as

$$\mathcal{H}(P, Q) = \sqrt{\frac{1}{2} \sum_{k=1}^K \left(\sqrt{\frac{1}{N} \sum_{i=1}^N \mathbb{I}(p_i = k)} - \sqrt{\frac{1}{M} \sum_{i=1}^M \mathbb{I}(q_i = k)} \right)^2}, \quad (2)$$

where $\mathbb{I}(\cdot) \in \{0, 1\}$ is the indicator function.

For d -dimensional continuous variables, $p_i, q_j \in \mathbb{R}^d$, we use the Wasserstein distance (otherwise known as the earth-mover’s distance). In its general form, the Wasserstein distance between two distributions $p(x)$ and $q(x)$ is given by the cost of the optimal transport plan that moves the probability mass of $p(x)$ to $q(x)$, where the cost is defined as equal to the amount of probability mass moved multiplied by distance moved in the underlying space²². For empirical distributions, where the distribution is formed of point masses at sample points $P = \{p_i\}_{i=1}^N$ and $Q = \{q_j\}_{j=1}^M$, the optimal transport plan, and therefore Wasserstein distance, may be found by computing Euclidean distances between all pairings of points in P and Q , and solving

the following linear program:

$$\begin{aligned}
\mathcal{W}(P, Q) &= \min_{\gamma} \sum_{i=1}^N \sum_{j=1}^M \gamma_{i,j} \|p_i - q_j\|_2 \\
\text{s.t. } & \sum_{i=1}^N \gamma_{i,j} = \frac{1}{M}, \quad j = 1, \dots, M \\
& \sum_{j=1}^M \gamma_{i,j} = \frac{1}{N}, \quad i = 1, \dots, N \\
& 0 \leq \gamma_{i,j} \leq 1, \quad i = 1, \dots, N, j = 1, \dots, M
\end{aligned} \tag{3}$$

where $\gamma_{i,j} \in \mathbb{R}$ is the quantity of probability mass moved from initial point p_i in the first distribution to end point q_j in the second distribution. In our implementation, we use the open-source Python Optimal Transport (POT) library²³ to calculate the solution to this optimal transport problem.

By using the Hellinger distance, we obtain a symmetric and bounded measure of dissimilarity between discrete distributions that is sensitive to differences even when categories are missing or sample sizes are small. The Wasserstein distance allows us to capture differences in the overall shape and location of continuous distributions, including multivariate data, thereby detecting shifts in the joint distribution that the KS test would miss.

2.1.3 Uncertainty Bounds on Distance Metrics

The original ChexStray framework used a bootstrapping method wherein the data within the detection window was randomly oversampled to a fixed size in order to combat the sensitivity of metrics to sample size. This discards potentially useful information about the uncertainty that is introduced for low sample sizes.

With MMC+, we take a different approach to provide a measure of the uncertainty on distance metrics between the reference window R and a detection window W . We perform the following sampling method, inspired by the Flapjack algorithm²⁴. We first draw two independent sets of samples randomly and uniformly from R without replacement: $U, V \subseteq R$, where the size of the subsets is determined by the size of W , i.e. $|U| = |V| = |W|$ which ensures that comparisons between these sets are fair and not biased by differing sample sizes. This requires that $|W| < |R|$ for all detection windows W , which in practice means choosing a sufficiently large reference window compared to the typical size of detection windows. This process is then repeated N_s times to generate multiple sampled subsets, $\{U_n\}_{n=1}^{N_s}$ and $\{V_n\}_{n=1}^{N_s}$. These subsets of samples are then used to calculate a set, D , containing estimates of the distance metric, calculated by comparing the distance between the W and U to the distance between V and U :

$$D(W, R) = \{d_n(W, R)\}_{n=1}^{N_s} = \{\mathcal{D}(U_n, W) - \mathcal{D}(U_n, V_n)\}_{n=1}^{N_s} \tag{4}$$

where \mathcal{D} is the distance metric for the particular variable (either Wasserstein distance for continuous variables or Hellinger distance for discrete variables). Here, subtracting $\mathcal{D}(U_n, V_n)$ serves as a baseline to account for the inherent variability within the reference window due to finite sampling. This adjustment isolates the true difference between W and R beyond what would be expected by chance. The number of samples to draw, N_s may be freely chosen to trade off accuracy and computational demands. For simplicity we omit the explicit dependence on R and W are implied and refer to the set of distance estimates simply as D .

We report the mean value of D over samples as the estimated distance and the minimum and maximum values across D to obtain an estimate of the uncertainty of the distance metric. Since MMC+ is composed of distance metrics from several components, we repeat this process for all components and calculate individual metrics for each the appropriate distance metric for each. We denote the distance measures for each of component with the superscript c and the c^{th} component as $d_n^{(c)}$. More formally:

$$\psi^{(c)} = \frac{1}{N_s} \sum_{n=1}^{N_s} d_n^{(c)}, \quad \langle \psi_U^{(c)}, \psi_L^{(c)} \rangle = \langle \max_n d_n^{(c)}, \min_n d_n^{(c)} \rangle \tag{5}$$

where $\psi^{(c)}$ is the mean of $d_n^{(c)}$ which we take to be the raw individual distance metric for c^{th} component, and $\psi_U^{(c)}$ and $\psi_L^{(c)}$ are the maximum and minimum values of $d_n^{(c)}$ over all samples $n = 1, \dots, N_s$.

2.1.4 Multi-Modal Concordance (MMC+)

The MMC+ metric combines distance metrics from multiple from C components into a single metric. Since, the metrics for each component have different ranges, we first normalize them. For the c -th component, we calculate normalization parameters

by finding the mean $\zeta^{(c)}$ and standard deviation $\eta^{(c)}$ of the distance metric $\psi^{(c)}$ between each possible detection window W_k within the reference set R and the remainder of the reference set \hat{R}_k , defined as:

$$\hat{R}_k = \{x_i \mid x_i \in R, x_i \notin W_k\} \quad (6)$$

In addition to normalization, we weight each component to reflect its importance or reliability in the final unified score. For component c , we calculate a weight value $\alpha^{(c)}$ based on the absolute value of the Pearson correlation coefficient (ρ) between the model performance and the distance metric. Here, performance is measured using the area under the receiver operating characteristic curve (AUROC), denoted as $a(W_k)$, where W_k represents each detection window within the reference set R . Like the normalization calculation, the distance metric is computed between W_k and the remainder of the reference set, \hat{R}_k . The weight is computed as:

$$\alpha^{(c)} = \left| \rho \left(\psi^{(c)}(W_k, \hat{R}_k), a(W_k) \right) \right| \quad (7)$$

Combining the normalized and weighted component distances, we calculate the multimodal concordance metric (MMC+) the detection window W as

$$\text{MMC+} = \sum_{c=1}^C \alpha^{(c)} \frac{\psi^{(c)} - \zeta^{(c)}}{\eta^{(c)}} \quad (8)$$

To account for uncertainty, we also compute the upper and lower bounds of MMC+ denoted as

$$\langle \text{MMC+}_U, \text{MMC+}_L \rangle = \sum_{c=1}^C \alpha^{(c)} \frac{\langle \psi_U^{(c)}, \psi_L^{(c)} \rangle - \zeta^{(c)}}{\eta^{(c)}} \quad (9)$$

Here, MMC+_U and MMC+_L are the upper and lower bounds of the distance metric for component c , obtained from the uncertainty estimates as described in the previous section. By weighting each component according to its correlation with model performance, we emphasize metrics that are more predictive of performance changes, enhancing the sensitivity and reliability of MMC+. The upper and lower bounds provide a range for MMC+, offering insight into potential variability due to sampling or measurement uncertainties.

2.2 Dataset

Our dataset was created by querying an institutional radiology database at Massachusetts General Hospital for all imaging studies matching the following criteria: 1) modality of “XR” (X-ray), 2) an institution-specific examination code with one of two values corresponding to “X-Ray Chest 1 View” and “X-Ray Chest PA And Lateral 2 Views”, 3) a study date from within the two-year period between 2019-07-01 and 2021-07-01 (“yyyy-mm-dd” format, inclusive), and 4) patient age of 18 years or older. This dataset was chosen to reflect the full set of studies that would likely be routed to an X-ray analysis model if it were deployed in clinical practice at Massachusetts General Hospital, as well as to capture the period of time before, during, and after the initial wave of the COVID-19 pandemic.

This process yielded 90,713 studies of which 90,581 (from 60,062 distinct patients) were successfully retrieved from the institutional Picture Archive and Communication System (PACS) along with their radiology reports. To create ground truth labels for this dataset, we used a large language model (Qwen 1.5-72B) to extract labels for each of a set of nine findings by few-shot prompting the model with a small number of positive and negative examples. We characterized the accuracy of this process on a subset of this same dataset in previously published work²⁵, and found it to be highly accurate for most findings. Following the Chexpert convention²⁶, the nine selected findings were: atelectasis, cardiomegaly, edema, lung opacity, pleural effusion, pleural other, pneumonia, pneumothorax, and support devices. We excluded the following findings due to inconsistency when extracting ground truth labels: consolidation, enlarged cardiomedastinum, fracture, lung lesion, and “no finding”. We note that ground truth labels were required to assess the relationship of drift metrics to performance, but would not be required to use the MMC+ framework to monitor for drift in practice.

We divided the dataset into three subsets based on the date of acquisition as follows: studies acquired in the first three months (July 2019 through September 2019) were used for model training and validation, studies from the next three months (October 2019 through December 2019) were used as reference set for the drift metric, and the remaining studies covering an 18-month period from the start of January 2020 until the end of June 2021 were used for the drift experiments. This division was chosen to approximately reflect a model development process. In such a process a model would first be developed on retrospective images, then validated on recent images before being deployed prospectively on new images.

	Training	Reference	Test
Start Date	2019-07-01	2019-10-01	2020-01-01
End Date	2020-09-31	2020-12-31	2021-07-01
Age (years, mean \pm std)	60.2 ± 18.48	59.53 ± 18.22	58.64 ± 17.87
Female (%)	48.12	49.44	46.03
Inpatient (%)	14.74	14.44	27.84
Emergency (%)	31.53	29.37	27.68
Portable (%)	28.15	27.79	51.38
Total Images	12,478	14,936	78,181

Table 1. Summary of dataset characteristic statistics.

2.3 Classification Model

For the purposes of our experiments, the AI model whose performance we monitored was a classification model trained to detect multiple findings in a chest radiograph. This model was based on the DenseNet-121 architecture, pretrained on ImageNet-1k dataset^{27,28}. The output layer was adapted to consist of nine elements, one for each of the nine findings, followed by a sigmoid activation to yield nine independent (multi-label) predictions. The model was trained on the images from the training set, defined in Section 2.2. Training was conducted with a batch size of 64, a learning rate of 1×10^{-4} , a binary cross-entropy loss function, the Adam optimizer and a ReduceLROnPlateau learning rate schedule. The model was trained exclusively on frontal (AP and PA) images (lateral views were excluded) across all points of care. Training was performed using a single A100-40GB GPU (NVIDIA, Santa Clara, CA, USA).

2.4 MMC+ Data Elements

MMC+ is a general framework and can be used with a variety of different measurements from the datastream. In this section, we describe our setting for our experimental studies using the chest X-ray diagnostic model. With minor adjustments for the specifics of a particular image type and clinical application, the same framework can be used for any radiology-based ML model.

2.4.1 Imaging Metadata

Every radiological image acquired in clinical practice is stored within a standardized DICOM (Digital Imaging and Communications in Medicine) file alongside various metadata attributes that describe acquisition parameters of the image, patient characteristics, and the clinical context of the acquisition. For our experiments, we selected a number of DICOM attributes that may affect model performance on chest radiographs and used each as an individual element within MMC+. A small number of additional attributes were sourced from the institutional Radiology Information System (RIS). Table 2 lists the relevant attributes.

2.4.2 Image Appearance

In our previous implementation, we used a 128-dimensional latent vector produced by a VAE to represent the appearance of medical images. The VAE was trained on chest radiographs from the PadChest dataset²⁹, and the resulting latent vector served as the basis for calculating distance metrics to monitor shifts in image data. While this approach provided a functional, low-dimensional representation, it posed several challenges. Training the VAE required significant computational resources and data preparation which when in operation would need to be repeated at each site. Moreover, the VAE's limited expressiveness made it insufficient for capturing the complexity of medical images, particularly across imaging modalities.

To overcome these limitations, we transitioned to using MedImageInsight³⁰, a foundation model designed specifically for medical image analysis, which provides a 1024-dimensional embedding. Unlike the VAE, MedImageInsight does not require site-specific training, offering a powerful pre-trained solution that can be applied to a wide range of medical images out of the box. The larger 1024-dimensional embedding is significantly more expressive, capturing a richer and more detailed representation of image appearance, enabling the system to better generalize across various clinical settings and imaging modalities.

By leveraging MedImageInsight's pre-trained, high-dimensional embeddings, we eliminate the need for extensive, site-specific training processes, simplifying deployment and reducing the operational complexity of maintaining the system across different locations. MedImageInsight's generalizability allows it to adapt seamlessly to new imaging environments and protocols without requiring retraining, which not only enhances the robustness and accuracy of our image appearance monitoring framework but also ensures the system is more scalable and easier to maintain. This transition ultimately reduces the operational burden, making the system more efficient in real-world clinical environments.

Tag	Keyword	Type	Description
0008,0060	Modality	Discrete	DX “Digital Radiography” or CR “Computed Radiography”.
0008,0070	Manufacturer	Discrete	Manufacturer of the scanner that acquired the image.
0008,1090	ManufacturerModelName	Discrete	Model name of the scanner that acquired the image.
0010,0040	Patient Sex	Discrete	Sex of the patient.
0018,0060	KVP	Continuous	Kilo-volt peak of the source X-Ray tube.
0018,1151	XRayTubeCurrent	Continuous	Current of the source X-Ray tube.
0018,1153	ExposureIn μ As	Continuous	Radiation exposure in μ As.
0018,5100	ViewPosition	Discrete	Radiographic view (e.g. posterior/anterior, lateral).
0028,0004	PhotometricInterpretation	Discrete	Interpretation of pixel data.
0028,0010	Rows	Continuous	Number of rows in the image.
0028,0011	Columns	Continuous	Number of columns in the image.
0028,0030	PixelSpacing	Continuous	Physical spacing between pixels.
0028,0101	BitsStored	Discrete	Pixel bit-depth.
(RIS)	Patient Age	Continuous	Age of the patient in years.
(RIS)	Point of Care	Discrete	Hospital location.
(RIS)	Is Stat	Discrete	Whether image was marked for urgent review.
(RIS)	Exam Code	Discrete	Internal procedure code (see Section 2.2).

Table 2. Table of DICOM and RIS attributes used for experiments including the tags, keywords, types (discrete or continuous), and descriptions of the data fields utilized in the analysis. These attributes include both imaging metadata (e.g., modality, exposure, pixel data) and patient-specific information (e.g., age, sex, point of care).

2.4.3 Model Predictions

The raw classifier output (after the sigmoid activations) consists of 9 independent values in the range 0–1, one for each of the findings. These values carry information about both the likely class distribution of the datastream and the model’s confidence in its predictions. This nine element vector is used directly as a multidimensional variable for calculating a single distance metric (the Wasserstein distance) for model predictions.

3 Results

We conducted various experiments to demonstrate the use of MMC+ on a representative, real-world dataset. For all the experiments presented in the following sections, we used a window duration τ of 30 days and a window stride δ of 1 day. We chose this window duration as a balance between minimizing lag time and addressing the noise and other issues that arise with smaller sample sizes, even though this choice can introduce some delay in drift detection. The number of resampling iterations, N_s , was set to 20.

3.1 MMC+ Results on Real-World Data

To evaluate the effectiveness of the MMC+ framework in detecting data drift and its relationship to model performance, we applied MMC+ to a real-world dataset of chest radiographs collected over an 18 month period that includes the onset of the COVID-19 pandemic. This experiment aims to simulate a realistic scenario where an AI model faces significant shifts in data distribution, allowing us to assess how MMC+ responds to such changes and whether it can serve as a reliable indicator for initiating performance audits or model updates.

Figure 2 shows the MMC+ over time starting from November 1st, 2019, which marks the end of the first complete 30 day window within the reference set, until July 1st, 2021. The MMC+ metric remains steady for approximately the first 2 months but increases rapidly in mid March 2020. This also coincides with the declaration of the state of emergency in the state of Massachusetts on March 10, 2020 due to the COVID-19 pandemic¹. Thereafter, MMC+ fluctuates but always remains high, suggesting that the data never returns to its initial characteristics following the onset of the pandemic. From Figure 3 we see how individual component groups contribute to MMC+ (metadata, image appearance, and model output). All of these component groups show a similar trends, suggesting all groups detect the dramatic changes.

Next, we examine the model’s performance in Figure 4, which depicts the AUROC for the individual findings across the same time period. We notice that nearly all performance indicators show some change starting in mid-March 2020, though they vary in scale and direction.

¹<https://www.mass.gov/info-details/covid-19-state-of-emergency>

Starting with the most significant changes, we see that the performance for cardiomegaly drops significantly and remains low throughout the period. In contrast, pleural other initially shows an increase in performance but then dips around June 2020. We also observe that the performance for lung opacity improves starting in May 2020, despite significant changes in the data.

The remaining differences in performance are more subtle but still apparent. We see minor increases in performance for atelectasis and pneumonia. Findings such as edema, pleural effusion, support devices, and both averages (macro and micro) exhibit performance swings in both directions during this time period, indicating instability in model predictions.

Regarding pneumothorax performance, we observe large fluctuations within the performance curve. However, since the performance of predicting this finding also varied widely in the reference set, it is challenging to determine if these changes are connected to data drift or are due to inherent variability in the model's predictions for this condition.

These observations highlight the complex relationship between data drift and model performance. While MMC+ effectively detects shifts in the data distribution, the impact on model performance is not uniform across different findings.

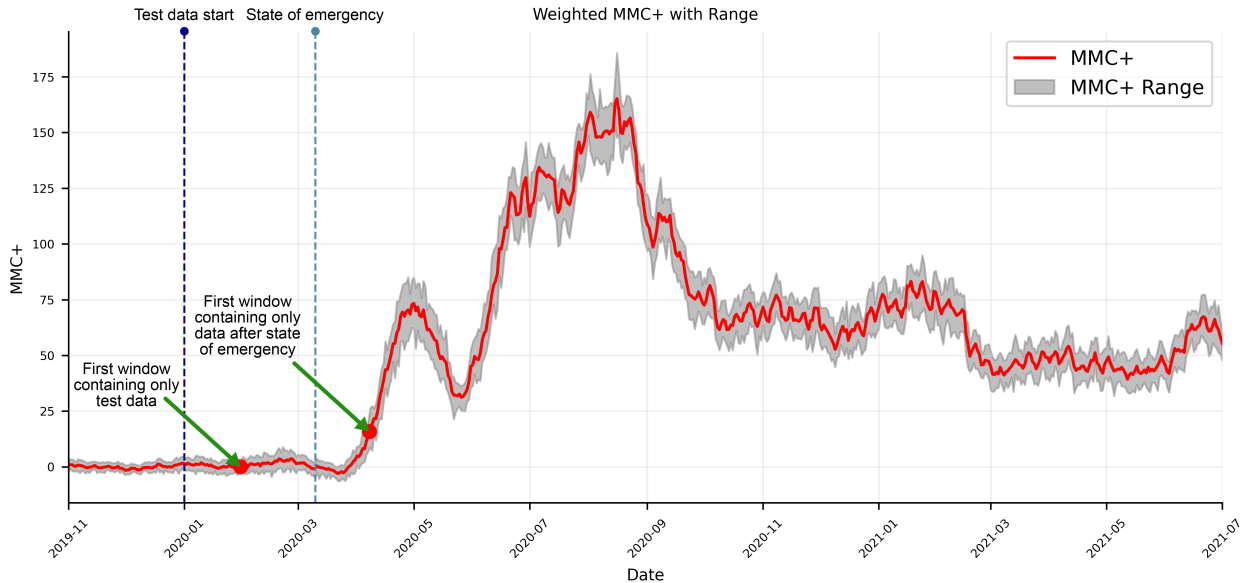


Figure 2. Plot of the evolution of MMC+ over time from 2019-11 to 2021-07. The red line depicts the weighted MMC+ value and the gray shaded area indicates the range or variability around the MMC+, providing the uncertainty in the MMC+ measurement during this time period. Two dashed vertical lines are shown: the first marks the start of the test data, and the second represents March 10, 2021, the day Massachusetts declared a state of emergency. Two arrows highlight the first windows where all data is sourced from either the test data or post-state-of-emergency period, a consequence of the window duration.

3.2 Relationship between MMC+ and performance

To assess the relationship between the MMC+ metric and performance consistency, we evaluated how MMC+ values correspond to the normalized AUROC across nine different labels, as well as micro and macro averages. Performance variability was observed across all datastreams, which prompted the calculation of “normal” fluctuations based on AUROC values from the reference set. These values were collected in 30 day windows to calculate the mean and standard deviation, which were subsequently used to normalize AUROC during the test period.

Each subfigure in Figure 5 presents a scatter plot where the x-axis represents the MMC+ value and the y-axis corresponds to the normalized AUROC for a different label. Data points are color-coded based on whether they occur before or after the onset of the pandemic (defined as the March 10 declaration of emergency in the state of Massachusetts), with the edges of each scatter plot displaying a kernel density estimate (KDE) of the two groups to highlight any separation.

A clear pattern emerges from these figures: when MMC+ values are within a certain range (less than 10 in this case), the normalized AUROC remains consistently within 3 standard deviations of the reference set mean. However, when MMC+ exceeds this range, the likelihood of the normalized AUROC remaining within 3 standard deviations of the reference mean diminishes significantly. Although performance does not universally decline—performance for some labels, such as Atelectasis, even improves in certain instances—the variability in performance increases notably. This indicates that while MMC+ remains

within its normal range, performance consistency is maintained, but outside this range, the model’s reliability becomes less predictable. In other words, high MMC+ is a sensitive but not specific indicator of performance shifts.

These observations are further supported by summary statistics presented in Table 3. Across the board, we observe greater variation in performance when MMC+ is outside its normal range. Furthermore, in all cases except for Pneumothorax which varies a great deal in the reference set, there is an increased proportion of AUROC values that deviate more than 3 standard deviations from the reference mean, underscoring the importance of maintaining MMC+ within its optimal range for consistent model performance.

Label	MMC+ < 10	MMC+ >= 10
Atelectasis	0.907	0.385
Cardiomegaly	0.711	0.049
Edema	0.845	0.810
Lung Opacity	0.825	0.100
Pleural Other	0.979	0.487
Pleural Effusion	1.000	0.885
Pneumonia	0.907	0.507
Pneumothorax	1.000	1.000
Support Devices	1.000	0.836

Table 3. Rates at which AUROC remains within 3 standard deviations of the reference set AUROC for various conditions across two MMC+ ranges (<10 and >=10), highlighting how the model’s performance varies for different conditions as MMC+ increases.

3.3 Monitoring at Separate Points of Care

Hospitals typically use a wide range of X-ray machines at different points of care, such as operating rooms, emergency departments, and outpatient clinics. Each of these points of care may experience data drift events differently, as they often deal with distinct patient populations, imaging protocols, and workflows. Monitoring drift separately at each point of care is therefore crucial to gaining a complete and nuanced understanding of drift events. Figure 6 illustrates the behavior of the MMC+ metric for two different points of care within the Massachusetts General Hospital system.

Figure 6a shows the MMC+ metric for the emergency room, where a pronounced drift event occurs around the onset of the COVID-19 pandemic. This drift mirrors the broader trend observed in the overall MMC+, with the onset of the pandemic causing a sharp change in the datastream. By contrast, Figure 6b shows the MMC+ metric for an operating room in the ambulatory care center. Here, the drift pattern is noticeably different. Although the data changes around the same time, the drift is marked by a broadening of the uncertainty bounds indicating a reduction in the number of studies performed. Additionally, a 50-day gap in data collection follows, after which the data resumes without a sustained drift. This also showcases the importance of uncertainty bounds.

3.4 Utility of metadata

Figure 7 demonstrates the importance of incorporating metadata attributes into the monitoring framework. Specifically, the figure highlights a significant shift in the distribution of the “View Position” attribute for X-ray acquisitions starting around June 2020. Initially, less than 20% of the images were captured using the antero-posterior (AP) projection, but by mid-2020, this proportion had increased to over 40%. The heart and mediastinum appears larger on AP images than on PA images due to the increased distance to the image receptor and beam divergence, which negatively impacts the diagnostic quality of these images for cardiomegaly, an enlarged heart. Figure 7 shows that this shift in the proportion of the view position is accompanied by a notable decline in the model’s performance for detecting cardiomegaly.

3.5 Comparison to P-value Based Methods

Several other methods for monitoring for data drift track the *p*-value of a statistical hypothesis test between the data within a detection window and that in the reference set. For example Kore et al.²⁰ monitor data drift using the *p*-value given by the mean maximum discrepancy (MMD) non-parametric two sample hypothesis test. In Figure 8, we followed this approach to explore the behavior of MMD on our dataset. Like in Kore et al. the MMD metric was calculated on the image appearance vector, found in our case with MedImageInsight, concatenated with the vector of model output scores.

Monitoring the *p*-value in the absence of the effect size, especially when the number of samples can be very large, is very sensitive to distribution shifts that are likely inconsequentially small in practice, but statistically significant. In real-world data,

this results in plots that appear volatile and difficult to interpret. By contrast, we find that distance metrics, accompanied by appropriate uncertainty bounds, give a single value that better lends itself to an intuitive visualization of data drift.

3.6 Re-calibration after Drift

One of the operational challenges in deploying AI models in clinical settings is the inevitability of data drift. Over time, the input data characteristics will shift, leading to changes in model performance. Eventually, these shifts stabilize, creating a new “normal” state. In such scenarios, consider a situation where data at a specific site has drifted, prompting an audit. Following this audit, necessary IT operations or model modifications are implemented to ensure that the model’s performance returns to an acceptable range. However, to ensure continued monitoring effectiveness in this new data environment, it becomes essential to re-calibrate the MMC+ metric to track changes from this new reference set.

This re-calibration is achieved by creating a new reference set using data from the audited period and recalculating the relevant weights and normalization factors. Our analysis as shown in Figure 9 demonstrates that this approach is effective, as it successfully adjusts the MMC+ metric back into its acceptable range, thereby restoring model stability and ensuring consistent performance in the newly stabilized data environment.

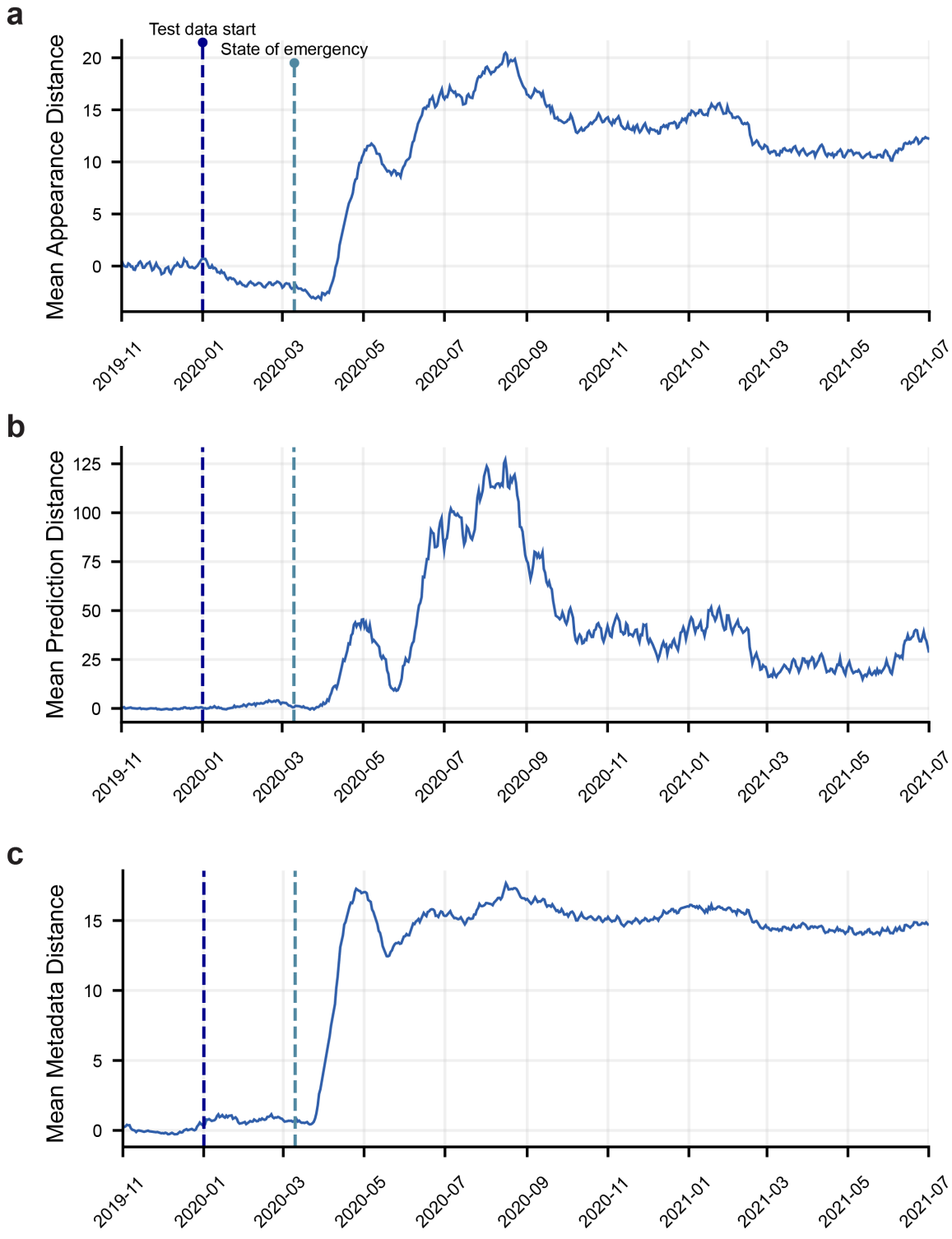


Figure 3. Plot of the evolution of MMC+ sub-components over time from 2019-11 to 2021-07. The MMC+ metric is composed of three high level components that capture data drift: a) the appearance metric represents changes in the appearance of medical images as encoded by the MedImageInsight foundation model, b) the model prediction metric captures shifts in model predictions from a trained classifier providing changes in the model's output over time, and c) the metadata metric measures variations in the extracted from the DICOM files and RIS systems.

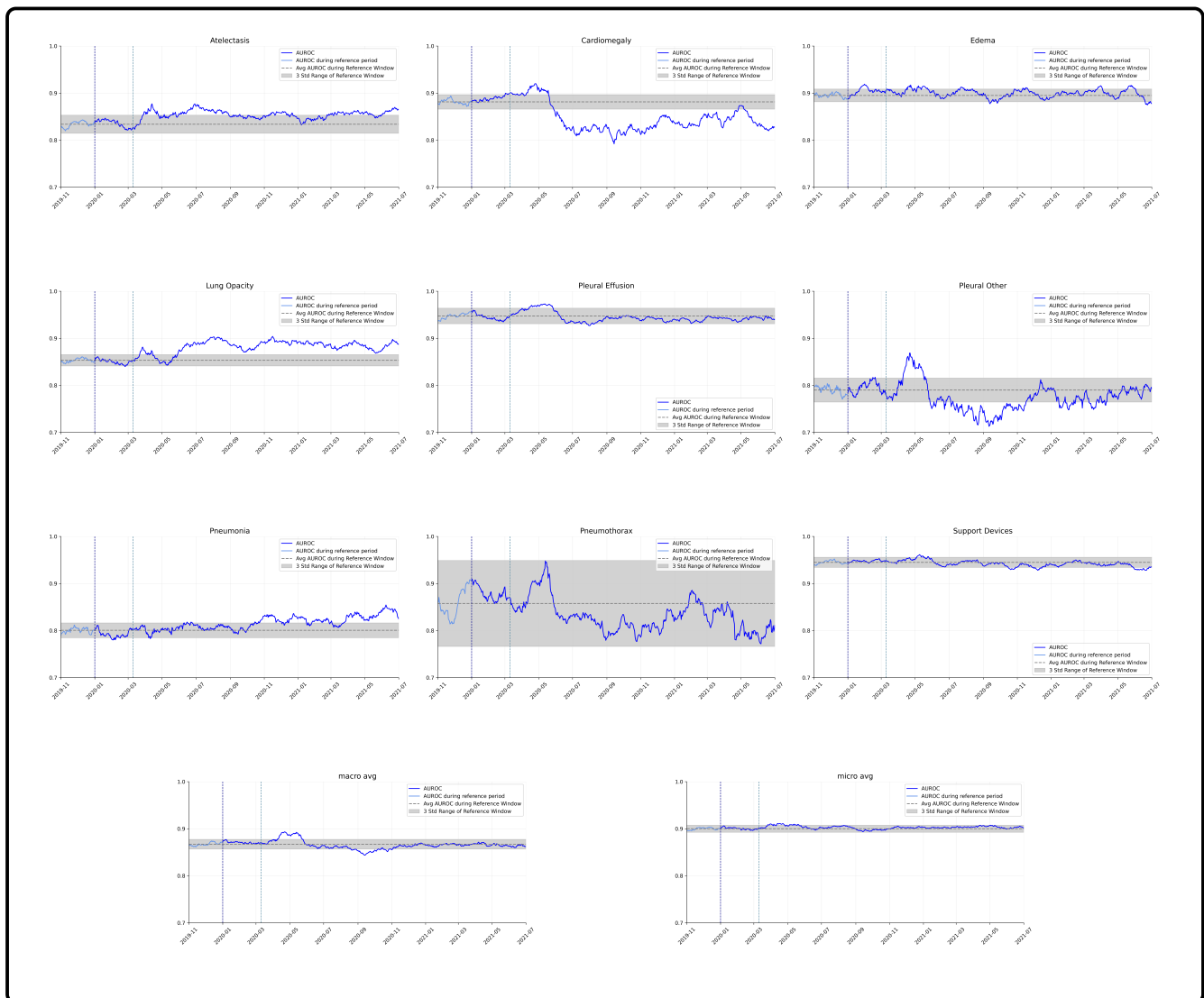


Figure 4. Plot of model performance (AUROC) for the nine findings and the macro/micro averages. AUROC is marked in blue, with the average performance during the reference period shown as a solid grey line and the reference period's 3 standard deviation range as a grey shaded area for each finding.

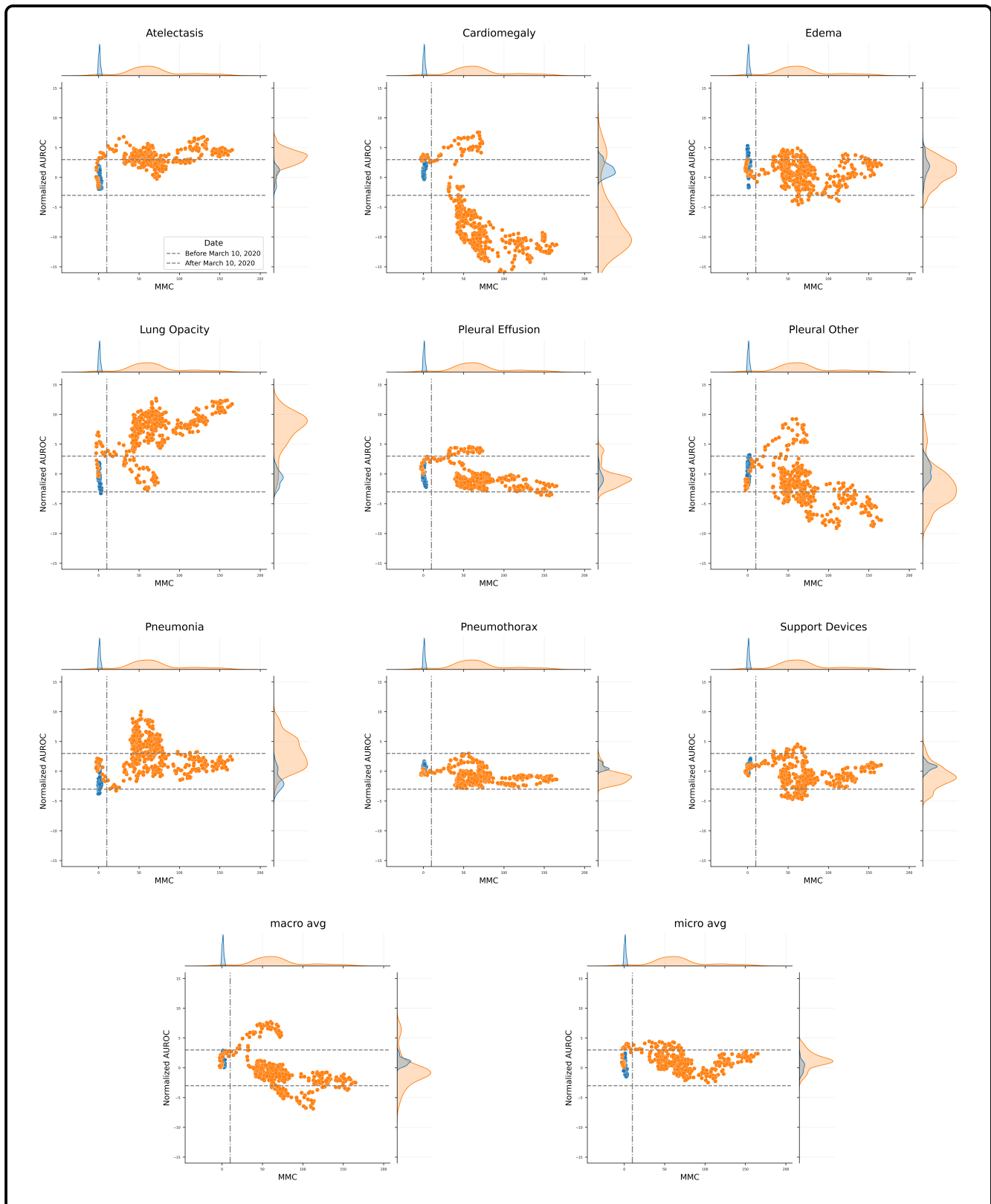
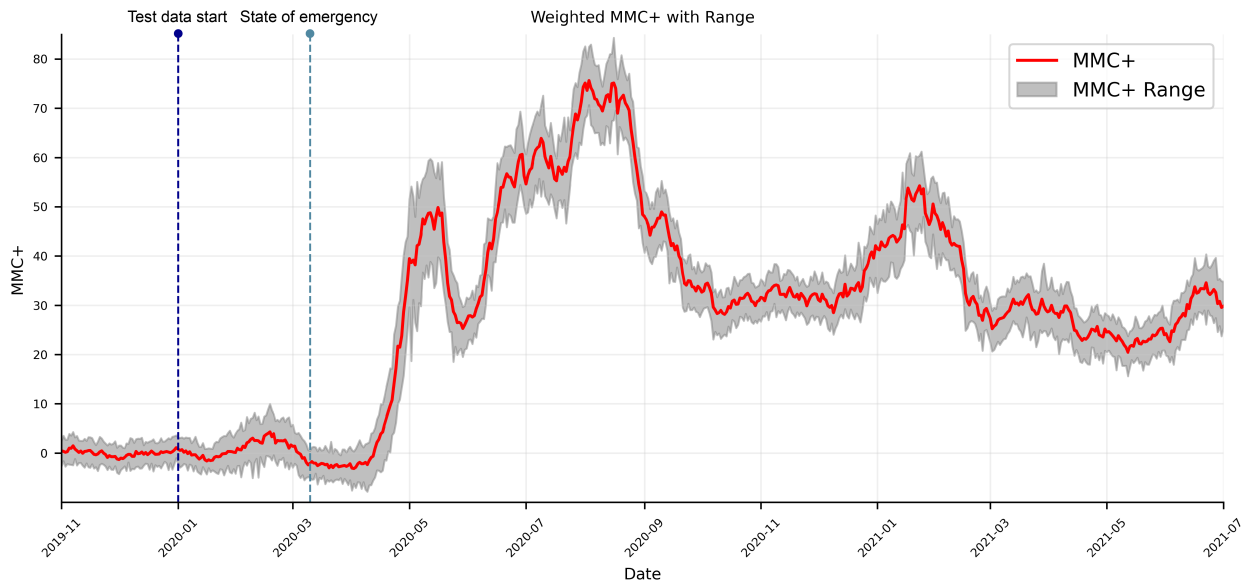
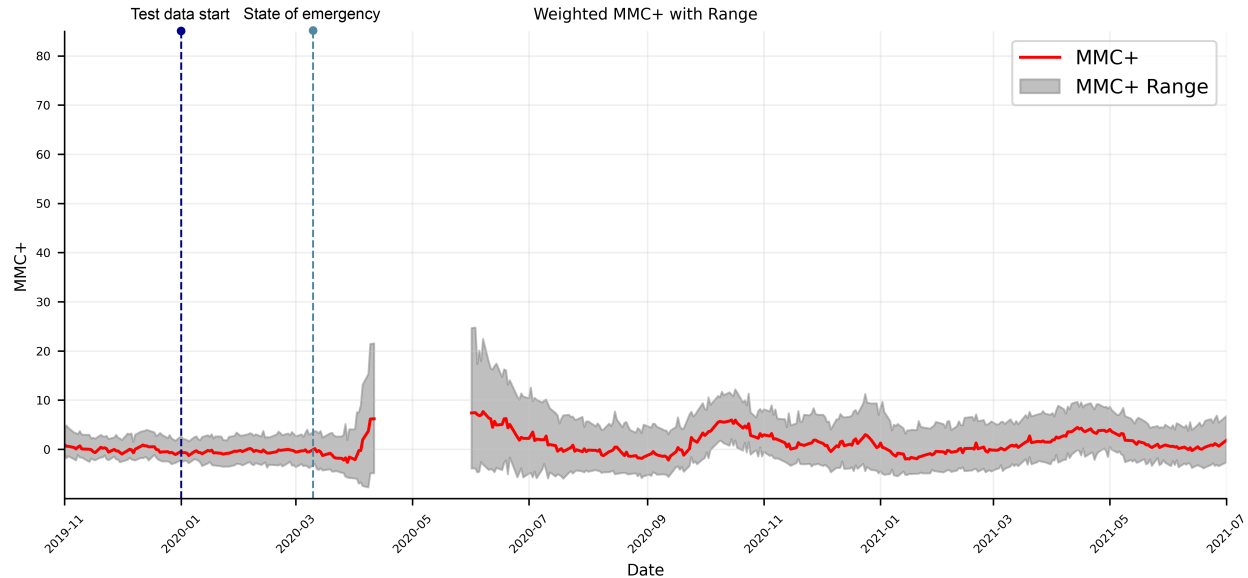


Figure 5. Relationship between MMC+ and normalized AUROC (standard deviation of AUROC) for each finding. In each plot, the blue points represent test set data before March 10, 2020, while the orange points represent data after this date. The horizontal dotted lines mark ± 3 standard deviations of the AUROC, and the vertical line at MMC+ = 10 represents the threshold where drift is observed. Above each scatter plot, KDE plots for the MMC+ and normalized AUROC are displayed, showing the distribution of test data pre- and post-March 10 (blue for pre, orange for post). These plots highlight the separation between the two time periods based on both MMC+ and AUROC behavior.



(a) MMC+ over time for the ER Point of Care



(b) MMC+ over time for the ambulatory center operating room Point of Care

Figure 6. Plots that show the evolution of MMC+ over time for two different points of care: (a) the ER Point of Care and (b) the ambulatory center operating room Point of Care. In both, the red line represents the weighted MMC+ values, while the gray shaded area indicates the range or variability around the MMC+.

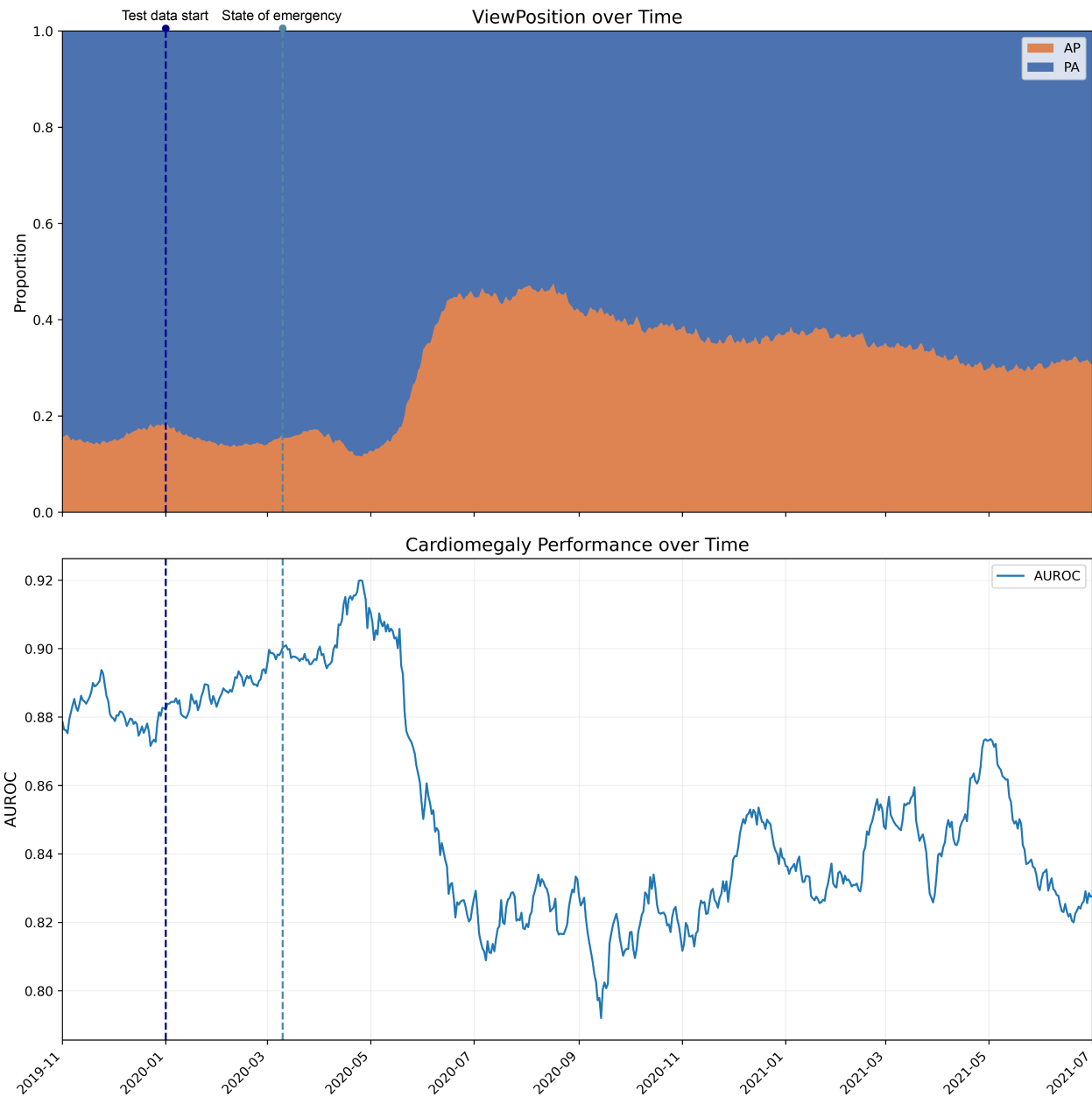


Figure 7. Comparison of View Position distribution and cardiomegaly performance over time as measured by AUROC. The top plot shows the distribution of View Position (AP and PA), and the bottom shows cardiomegaly performance. In both, the dashed vertical line marks March 10, 2020

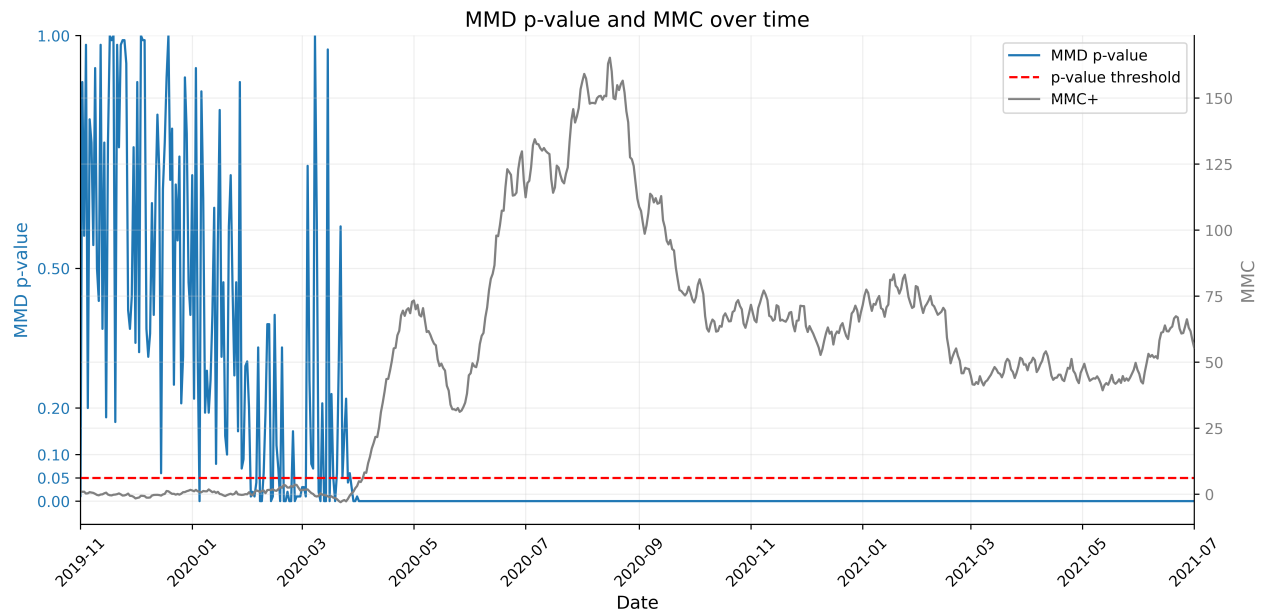


Figure 8. Comparison of MMD-based p-value and MMC+ over time. The blue line represents the MMD p-value, while the black line tracks the MMC+ values over the same period. The red dashed line indicates the p-value threshold (set at 0.05).

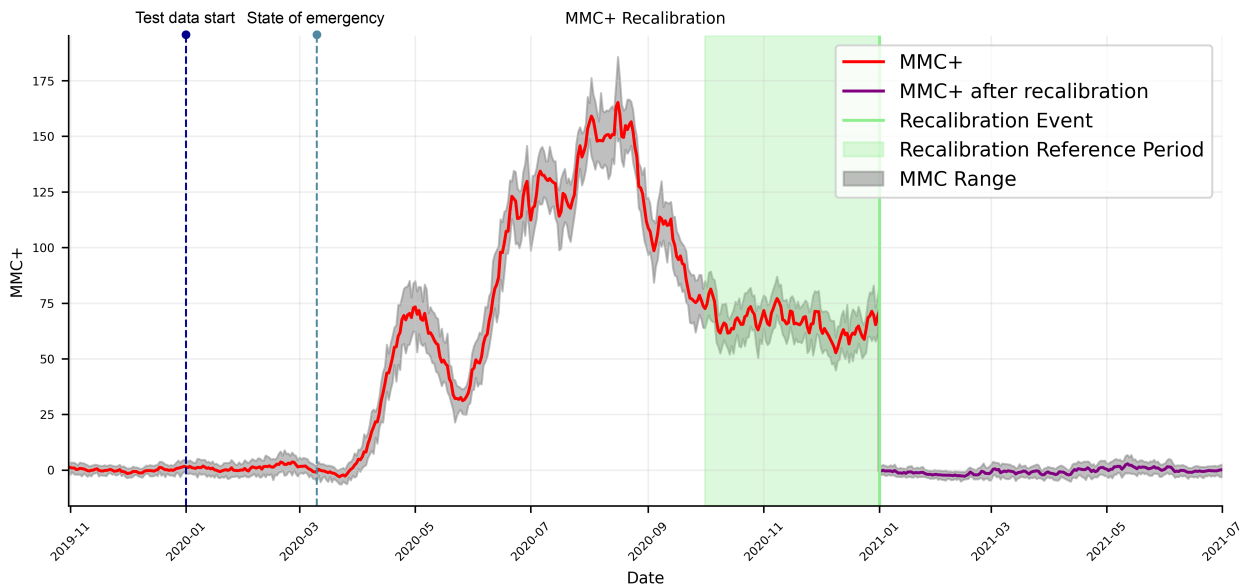


Figure 9. Plot of MMC+ over time with a re-calibration event. MMC+ recalibration on January 1st, 2021, using a new reference window from October 1st, 2020, to December 31st, 2020. The red line shows MMC+ values before recalibration, and the purple line indicates MMC+ values after recalibration. The grey shaded area represents the MMC+ range or variability. The recalibration event is marked by the vertical line, with the recalibration reference period highlighted in green.

4 Discussion

Our work addresses the pressing need for continuous monitoring in medical imaging AI applications. The rapid integration of AI into imaging demands evaluation methods that extend beyond initial validation stages. Ongoing, interpretable monitoring is essential to promptly detect issues such as model drift, feature drift, and shifts in input data. Current practices, which often rely on infrequent reviews and user feedback, are insufficient. They are too slow to respond to emerging problems and lack the depth required to understand the nuances of model behavior. Real-time performance monitoring, while ideal, is frequently cost-prohibitive and may not effectively identify the underlying causes of performance changes.

Existing monitoring tools are not well-suited for imaging data due to the complexity of image representations. Conventional methods like VAEs require extensive site-specific training and are challenging to scale across multiple locations, hindering widespread adoption. To overcome these limitations, we introduced MMC+, an enhanced drift detection system that incorporates uncertainty bounds, leverages MedImageInsight embeddings, and applies advanced metrics for more scalable and accurate monitoring. By utilizing foundation models like MedImageInsight, we reduce the need for retraining and simplify deployment, making the system more adaptable to various settings.

In our approach, we replace over-sensitive p -value calculations with more intuitive distance metrics such as Hellinger and Wasserstein distances that decouple effect size from sample size give a smoother quantification of the degree of data drift. These metrics are more robust even large sample sizes, whereas p -values can be misleading under those conditions.

As previous works have noted²⁰, our findings demonstrate that data drift does not invariably correlate directly to performance degradation; in some cases, performance may even improve. This underscores the importance of monitoring both the model outputs and the input data to gain a comprehensive understanding of the system's behavior. We observed that when MMC+ values remain within acceptable limits, the model's performance is stable. However, significant deviations in MMC+ warrant performance audits, model performance becomes unpredictable. We also observe that monitoring different operational sites (such as ER vs PostOp) separately, when feasible, can enhance detection accuracy and provide more granular insights into the model's performance across diverse datasets. We observed a clear connection between MMC+ values and model performance. Stable MMC+ values correspond to consistent performance levels, whereas large deviations in MMC+ result in variable and unpredictable performance. This insight is crucial as it offers a cost-effective compromise between continuous performance monitoring and periodic assessments.

In practical terms, hospitals can deploy MMC+ for continuous, real-time monitoring of AI models. This assists clinicians in identifying when AI support may be unreliable or require attention, thereby enhancing patient safety. However, obstacles remain. Existing methods might miss subtle yet important declines in model performance, and relying solely on proxies without verifying actual performance could compromise patient outcomes.

The wider impact and applicability of MMC+ are significant. The system has the potential to be used across different medical imaging modalities, stressing the importance of ongoing AI monitoring after deployment to ensure reliability. Incorporating uncertainty bounds aids in managing fluctuations in number of imaging studies over time and avoiding spurious drift measurements when data sizes are small. Transitioning to foundation models like MedImageInsight reduces retraining needs, enhancing scalability and ease of deployment. These foundation models could revolutionize monitoring by simplifying processes and reducing costs. Temporal assessment of abnormalities in context of changing acquisition techniques and radiographic quality along with evolving disease severity and developing and/or resolving coexisting comorbidities, is part of routine clinical interpretation of chest radiographs. Their impact on AI performance and the need for monitoring are thus of paramount importance. The highly subjective nature of projectional radiography and substantial inter-reader variations among radiologists underscore the importance of an automated and efficient real-time monitoring such as the MMC+. Such human observer variations often necessitate multi-reader participation which are both expensive and inefficient.

Our results highlight the limitations of monitoring data drift using p -values, particularly when large sample sizes amplify insignificant shifts that can lead to statistically significant but practically irrelevant results. This sensitivity, as seen with the MMD test, often leads to volatile and difficult-to-interpret plots. In contrast, distance metrics, such as Hellinger and Wasserstein, offer a more stable and intuitive representation of data drift by providing a single value that better captures meaningful changes in the data. These findings suggest that distance metrics present a more effective approach for tracking and visualizing data drift in real-world applications.

We acknowledge certain limitations in our study. The research focused mainly on chest X-ray data, and results may not generalize to other imaging types. MedImageInsight's generalizability requires validation across more diverse datasets, and assumptions regarding data characteristics and sample sizes may not hold in all settings. Future work should examine operational factors such as determining optimal thresholds for alerts and evaluate MedImageInsight on additional medical imaging tasks and datasets. Extending the application of MMC+ to three-dimensional imaging data like CT or MRI scans represents another avenue for exploration. Contextual factors such as adapting MMC+ for use in settings with limited computational resources and addressing regulatory considerations when deploying in different healthcare systems and regions are also important.

Another limitation of our study is the lack of validation in a broader set of common/contemporary clinical indications with

substantially reduced COVID-19 prevalence. However, given the non-specific nature of COVID-19 related findings on chest radiographs, and the scope of abnormalities from lungs to the bones assessed in our study, we believe that our results will be generalizable across other clinical indications.

MMC+ offers a scalable and effective approach for monitoring drift in medical imaging AI applications. By incorporating foundation models like MedImageInsight and utilizing advanced distance metrics, we enhance the accuracy and reliability of the monitoring system. Our approach addresses the limitations of existing methods by reducing the need for site-specific training and improving adaptability across various settings. Future efforts should focus on applying MMC+ to other imaging modalities, refining sensitivity to drift, and exploring operational considerations such as optimal alert thresholds. Overall, MMC+ advances dependable and scalable AI monitoring in the healthcare sector, contributing to improved patient outcomes and safety.

References

1. Merkow, J. *et al.* CheXstray: A Real-Time Multi-Modal Monitoring Workflow for Medical Imaging AI. In Greenspan, H. *et al.* (eds.) *Medical Image Computing and Computer Assisted Intervention – MICCAI 2023*, vol. 14222, 326–336, DOI: [10.1007/978-3-031-43898-1_32](https://doi.org/10.1007/978-3-031-43898-1_32) (Springer Nature Switzerland, Cham, 2023). Series Title: Lecture Notes in Computer Science.
2. van Leeuwen, K. G., Schalekamp, S., Rutten, M. J., van Ginneken, B. & de Rooij, M. Artificial intelligence in radiology: 100 commercially available products and their scientific evidence. *Eur. radiology* **31**, 3797–3804 (2021).
3. West, E., Mutasa, S., Zhu, Z. & Ha, R. Global trend in artificial intelligence-based publications in radiology from 2000 to 2018. *Am. J. Roentgenol.* **213**, 1204–1206 (2019).
4. Benjamens, S., Dhunnoo, P. & Meskó, B. The state of artificial intelligence-based fda-approved medical devices and algorithms: an online database. *NPJ digital medicine* **3**, 1–8 (2020).
5. Mehrizi, M. H. R., van Ooijen, P. & Homan, M. Applications of artificial intelligence (ai) in diagnostic radiology: a technography study. *Eur. radiology* **31**, 1805–1811 (2021).
6. Tadavarthi, Y. *et al.* The state of radiology ai: considerations for purchase decisions and current market offerings. *Radiol. Artif. Intell.* **2**, e200004 (2020).
7. Park, S. H. *et al.* Methods for clinical evaluation of artificial intelligence algorithms for medical diagnosis. *Radiology* **306**, 20–31 (2023).
8. Omoumi, P. *et al.* To buy or not to buy—evaluating commercial ai solutions in radiology (the eclair guidelines). *Eur. radiology* **31**, 3786–3796 (2021).
9. Feng, J. *et al.* Clinical artificial intelligence quality improvement: towards continual monitoring and updating of ai algorithms in healthcare. *npj Digit. Medicine* **5**, 66, DOI: [10.1038/s41746-022-00611-y](https://doi.org/10.1038/s41746-022-00611-y) (2022).
10. Rajpurkar, P. & Lungren, M. P. The current and future state of ai interpretation of medical images. *New Engl. J. Medicine* **388**, 1981–1990, DOI: [10.1056/NEJMra2301725](https://doi.org/10.1056/NEJMra2301725) (2023).
11. Panykh, O. S. *et al.* Continuous learning ai in radiology: implementation principles and early applications. *Radiology* **297**, 6–14 (2020).
12. Lacson, R., Eskian, M., Licaros, A., Kapoor, N. & Khorasani, R. Machine learning model drift: Predicting diagnostic imaging follow-up as a case example. *J. Am. Coll. Radiol.* **19**, 1162–1169 (2022).
13. Rahmani, K. *et al.* Assessing the effects of data drift on the performance of machine learning models used in clinical sepsis prediction. *Int. J. Med. Informatics* **104930**, DOI: [10.1016/j.ijmedinf.2022.104930](https://doi.org/10.1016/j.ijmedinf.2022.104930) (2023).
14. Ross, C. Ai gone astray: how subtle shifts in patient data send popular algorithms reeling, undermining patient safety. *STAT* (2022).
15. Daye, D. *et al.* Implementation of clinical artificial intelligence in radiology: who decides and how? *Radiology* **305**, 555–563 (2022).
16. Bizzo, B. C. *et al.* Addressing the challenges of implementing artificial intelligence tools in clinical practice: principles from experience. *J. Am. Coll. Radiol.* **20**, 352–360 (2023).
17. Subasri, V. *et al.* Cyclops: a unified framework for data extraction and rigorous evaluation of ml models for clinical use-cases. *Mach. Learn. for Healthc. 2022–Clinical Abstr. Software, Demo Track* (2022).
18. Duckworth, C. *et al.* Using explainable machine learning to characterise data drift and detect emergent health risks for emergency department admissions during covid-19. *Sci. reports* **11**, 23017 (2021).

19. Kingma, D. P. & Welling, M. Auto-encoding variational bayes. *arXiv preprint arXiv:1312.6114* (2013).
20. Kore, A. *et al.* Empirical data drift detection experiments on real-world medical imaging data. *Nat. Commun.* **15**, 1887, DOI: [10.1038/s41467-024-46142-w](https://doi.org/10.1038/s41467-024-46142-w) (2024).
21. Oosterhoff, J. & van Zwet, W. R. *A note on contiguity and Hellinger distance* (Springer, 2012).
22. Panaretos, V. M. & Zemel, Y. Statistical aspects of wasserstein distances. *Annu. review statistics its application* **6**, 405–431 (2019).
23. Flamary, R. *et al.* Pot: Python optimal transport. *J. Mach. Learn. Res.* **22**, 1–8 (2021).
24. Papp, T. & Sherlock, C. Bounds on wasserstein distances between continuous distributions using independent samples. *arXiv preprint arXiv:2203.11627* (2022).
25. Dorfner, F. J. *et al.* Is Open-Source There Yet? A Comparative Study on Commercial and Open-Source LLMs in Their Ability to Label Chest X-Ray Reports (2024). ArXiv:2402.12298 [cs].
26. Irvin, J. *et al.* Chexpert: A large chest radiograph dataset with uncertainty labels and expert comparison. In *Proceedings of the AAAI conference on artificial intelligence* (2019).
27. Huang, G., Liu, Z., van der Maaten, L. & Weinberger, K. Q. Densely connected convolutional networks (2018). [1608.06993](https://arxiv.org/abs/1608.06993).
28. Deng, J. *et al.* Imagenet: A large-scale hierarchical image database. In *2009 IEEE Conference on Computer Vision and Pattern Recognition*, 248–255, DOI: [10.1109/CVPR.2009.5206848](https://doi.org/10.1109/CVPR.2009.5206848) (2009).
29. Bustos, A., Pertusa, A., Salinas, J.-M. & de la Iglesia-Vayá, M. Padchest: A large chest x-ray image dataset with multi-label annotated reports. *Med. Image Analysis* **66**, 101797, DOI: [10.1016/j.media.2020.101797](https://doi.org/10.1016/j.media.2020.101797) (2020).
30. Codella, N. C. F. *et al.* Medimageinsight: An open-source embedding model for general domain medical imaging (2024). [2410.06542](https://arxiv.org/abs/2410.06542).